High Thermoelectric Performance in Supersaturated Solid Solutions and Nanostructured n-type PbTe-GeTe

Zhong-Zhen Luo, Xiaomi Zhang, Xia Hua, Gangjian Tan, Trevor P. Bailey, Jianwei Xu, Ctirad Uher, Chris Wolverton, Vinayak P. Dravid, Qingyu Yan,* Mercouri G. Kanatzidis*

Dr. Z. Z. Luo, Prof. Q. Y. Yan

School of Materials Science and Engineering

Nanyang Technological University

50 Nanyang Avenue, 639798, Singapore

E-mail: alexyan@ntu.edu.sg

Dr. Z. Z. Luo, Dr. G. J. Tan, Prof. M. G. Kanatzidis

Department of Chemistry

Northwestern University

Evanston, Illinois 60208, United States

E-mail: m-kanatzidis@northwestern.edu

X. M. Zhang, X. Hua, Prof. C. Wolverton, Prof. V. P. Dravid

Department of Materials Science and Engineering

Northwestern University

Evanston, Illinois 60208, United States

T. P. Bailey, Prof. C. Uher

Department of Physics

University of Michigan

Ann Arbor, Michigan 48109, United States

Prof J. W. Xu

Institute of Materials Research and Engineering

A*STAR (Agency for Science, Technology and Research)

2 Fusionopolis Way, Innovis #08-03, 138634, Singapore

Abstract We report Sb-doped and GeTe-alloyed n-type thermoelectric materials that show excellent figure of merit ZT in the intermediate temperature range (400-800 K). We demonstrate the synergistic effect of favorable changes to the band structure resulting in high Seebeck coefficient and enhanced phonon scattering by point defects and nanoscale precipitates resulting in reduction of thermal conductivity. The samples can be tuned as single-phase solid solution (SS) or two-phase system with nanoscale precipitates (Nano) based on the annealing processes. The GeTe alloying results in band structure modification by widening the band gap and increasing the density-of-states effective mass of PbTe, resulting in significantly enhanced Seebeck coefficients. The nanoscale precipitates can improve the power factor in the low temperature range and further reduce the lattice thermal conductivity (κ_{lat}). Specifically, the Seebeck coefficient of $Pb_{0.988}Sb_{0.012}Te$-13%GeTe-Nano approaches -280 μVK^{-1} at 673 K with a low κ_{lat} of 0.56 $Wm^{-1}K^{-1}$ at 573 K. Consequently, a peak ZT value of 1.38 is achieved at 623 K. Moreover, a high average ZT_{avg} value of ~1.04 is obtained in the temperature range from 300 K to 773 K for n-type $Pb_{0.988}Sb_{0.012}Te$-13%GeTe-Nano.

1. Introduction

Thermoelectric materials, which can convert heat to electricity and generate temperature gradients for cooling purposes, are attractive for clean and reliable energy harvesting technologies with reduced

hazardous gas emissions.[1] The effectiveness of a thermoelectric material is quantified by the dimensionless figure of merit $ZT = S^2\sigma T/\kappa$, where S is the Seebeck coefficient, σ is the electrical conductivity, T is the absolute temperature, and κ is the thermal conductivity (including the electronic and lattice components), respectively.[2] The quantity of $S^2\sigma$ is defined as the power factor, PF. High ZT can be achieved in materials that possess large power factor and low thermal conductivity.[2] Furthermore, power generation efficiency (η) of thermoelectric device is directly determined by the average ZT_{avg} over the operating temperature range, $\eta = [(T_H - T_C)/T_H] [(1 + ZT_{avg})^{1/2} - 1]/[(1 + ZT_{avg})^{1/2} + T_C/T_H]$, where T_H and T_C are the hot and cold junctions temperature, respectively. Considering medium-temperature waste heat sources (*e.g.* from 573 K to 722 K) account for about 70% of all the waste heat sources from 373 K to 873 K,[3] it is important to explore thermoelectric materials with high ZT values (especially ZT_{avg}) in the medium-temperature range.

P-type lead chalcogenide thermoelectric materials have outstanding medium-temperature thermoelectric performance, which is partly related to the intrinsic low thermal conductivity due to phonon anharmonicity[4] and partly to the unique two valence band (VB) electronic structure (light hole band at the L point and heavy hole band at the $\sum$ point).[5] As a results PbTe can easily achieve high power factors *via* VB convergence by alloying with other isovalent elements.[1b, 6] Effective state of the art strategies to enhance the power factor include tuning the electronic band structure near the Fermi level using resonant states,[7] band convergence,[8] multiple bands,[9] manipulating the band gap,[10] and band alignment using second phases,[11] Simultaneously, the thermal conductivity (mainly κ_{lat}) was reduced through all length-scale phonon scattering *via* the formation of hierarchical architecture or point defect scattering (i.e., solid solution alloying). [1c, 4a, 6a, 6f, 12]

The main reason for n-type PbTe lagging in thermoelectric performance is that it features only single conduction band (CB) at the L point which can participate in transport.[13] The smaller number of degenerate CB valleys than VB ones result in smaller electron effective mass and lower intrinsic Seebeck coefficient values.[14] Thus, the development of advanced n-type PbTe to match its p-type counterpart is a far more challenging task. Recently, the synergistic effect of co-doping strategies was demonstrated to progressively improve the ZT values for n-type PbTe.[15] For example, indium and iodine co-doped PbTe reaches a ZT value of 0.59 at 655 K.[16] Cl-doped $(PbTe)_{0.75}(PbS)_{0.15}(PbSe)_{0.1}$ exhibits a maximum ZT value of ~1.1 at 800 K.[17] $Pb_{0.98}In_{0.02}Te_{0.8}S_{0.2}$ has also been shown to achieve an enhanced ZT value of ~1.1 at 673 K by using a deep lying dopant.[18] Recently, high ZT ~1.5 at 723K was reported in PbTe-2%Cu_2Te by synergistically suppressing κ_{lat} and enhancing carrier mobility through Cu_2Te inclusions.[19]

Compared to cubic PbTe, GeTe crystallizes in a rhombohedral structure ($R3m$), which is stable up to ~700 K (called the α-GeTe phase) above which it becomes cubic.[20] Based on the concept of phase separation and nanostructuring, a very high ZT value of up to ~2 was obtained for Ge-rich p-type $Ge_{0.87}Pb_{0.13}Te$.[21] There are few studies about n-type GeTe alloyed PbTe system lying on the Pb-rich side of the phase diagram.[22] Here we report on the synergistic effect produced by a combination of Sb doping and GeTe alloying into the PbTe matrix that leads to enhance the n-type thermoelectric performance.

We describe a series of nominal compositions $Pb_{0.988}Sb_{0.012}$Te-x%GeTe (x = 0, 2, 5, 8, 10, 12, 13 and 14) solid solutions (SS) and nanostructured (Nano) $Pb_{0.988}Sb_{0.012}$Te-13%GeTe. We chose these compositions so we can study the solubility range to full supersaturation beyond the solubility range so

as to induce nucleation and growth to nanostructuring. The Sb doping and GeTe alloying brings the following advantages: (1) control of the carrier concentration in the range of ~1 to 5×10^{19} cm^{-3}, which is close to the optimum carrier concentration for achieving high *ZT* value; (2) enlargement of the band gap and electron effective mass leading to a considerable enhancement of the Seebeck coefficient; (3) the κ_{lat} is significantly reduced. Moreover, nanoscale precipitates improve the power factor at low temperature range and further reduce the κ_{lat}. Consequently, an enhanced *ZT* value of 1.38 at 623 K and a high average ZT_{avg} value of ~1.04 in the temperature range of 300 K to 773 K are achieved for Pb$_{0.988}$Sb$_{0.012}$Te-13%GeTe-Nano. These are among the highest ZT_{avg} values for n-type PbTe materials reported so far.

2. Results and Discussion

2.1. Sample Preparation

Polycrystalline solid solution samples of Pb$_{0.988}$Sb$_{0.012}$Te-x%GeTe, nanostructure sample of Pb$_{0.988}$Sb$_{0.012}$Te-13%GeTe and PbTe-x%GeTe (x = 0, 2, 5, 8, 10, 12, 13 and 14) were prepared *via* high temperature quenching and annealing of relative long duration. Furthermore, Sb as an amphoteric dopant in PbTe can be used as a substitute for either Te vacancies (at low doping levels of < 1%) or Pb sites (at higher doping levels of > 1%). Sb is a versatile choice to fine tune the carrier concentration and the lattice structures.[13, 20a], [23] In this study Sb doping amount of ~ 1.2% is chosen for tuning the carrier concentration of PbTe-x%GeTe to achieve high *ZT*. The GeTe content was varied from 2-14%. Because of the large mass fluctuation (Pb and Ge) in the crystal lattice, we hypothesized that by increasing the solid solubility of GeTe in PbTe matrix *via* high temperature annealing we can expect a significant reduction of the lattice thermal conductivity due to enhanced point defect scattering. Furthermore, considering the lower solid solubility at low temperature, we anticipated phase separation to occur at lower temperatures. Thus, we expected the formation of nanostructures *via* low-temperature annealing to further improve the thermoelectric performance by further reducing the lattice thermal conductivity through the scattering of mid-wavelength and long wavelength phonons.

2.2. Structural Characterization and Optical Properties

Figure S1 (Supporting Information) displays typical PXRD patterns of the Pb$_{0.988}$Sb$_{0.012}$Te-x%GeTe-SS (x = 0, 2, 5, 8, 10, 12, 13 and 14) samples. All patterns can be indexed to the cubic PbTe phase (JCPDS 78−1905) with the rock salt (NaCl) crystal structure (space group $Fm\bar{3}m$) without any other detectable impurity or secondary phase, suggesting the formation of a solid solution over the whole composition range of our study. The lattice constants obtained from the XRD patterns contract with increasing GeTe content, see Figure 1a. This is caused by the substitution of Pb^{2+} (~1.20 Å) cations by the smaller Ge^{2+} (~0.65 Å) cations. The trend follows Vegard's Law type behavior, which suggests the formation of a solid solution. In contrast, Pb$_{0.988}$Sb$_{0.012}$Te-13%GeTe-Nano (red) has larger lattice constant than that of Pb$_{0.988}$Sb$_{0.012}$Te-13%GeTe-SS, caused by lower solubility of GeTe. The band gap values increase from ~0.23 eV to 0.27 eV in going from 2% to 13% GeTe. These results are consistent with the larger band gap of GeTe (0.5 eV), see electronic absorption spectra in Figure 1b.[24]

2.3. Microstructure of the Solid Solution System

Microstructure information of the $Pb_{0.988}Sb_{0.012}Te$-13%GeTe-SS sample is summarized in Figure 2. Figures 2a-c depict very clear, homogeneous, single-phase microstructure. No obvious contrast for the presence of second phase can be observed, indicating that the material is a solid solution system. This is consistent with the Vegard's law type behavior observations shown in Figure 1a. The corresponding selective area electron diffraction (SAED) pattern along zone axis [001] is shown in the lower left inset picture of Figure 2a. The SAED pattern matches with rock-salt (NaCl) structure with the space group $Fm\bar{3}m$ No additional spots, spots splitting, streaking or super-lattice spots are observed in the SAED pattern. This demonstrates that the material is a single-phased system with no super-lattice structure and no secondary phase present. In Figure 2c, the measured lattice spacing (d_{200}) corresponds to the value calculated from PXRD (Figure 1a) within experimental error. Figure 2d is a representative EDS spectrum for $Pb_{0.988}Sb_{0.012}Te$-13%GeTe-SS from the homogeneous single phase. The spectrum demonstrates the existence of Pb, Te and Ge. The unlabeled peaks come from the TEM specimen holder or the TEM grid underneath the specimen. Figure 2e shows an HAADF STEM image with corresponding elemental maps of Ge, Pb, and Te. All three elements distribute uniformly throughout the observed region. The contrast in the elemental maps come from thickness variation.

2.4. Charge Transport Properties

Figure 3a describes the temperature-dependent electrical conductivity for $Pb_{0.988}Sb_{0.012}Te$-x%GeTe-SS. The electrical conductivity decreases with increasing temperature typical of degenerate semiconductors. At T = 300 K, the GeTe alloying reduces the electrical conductivities of the samples, *i.e.* from ~2885 Scm^{-1} for $Pb_{0.988}Sb_{0.012}Te$ to ~599 Scm^{-1} for $Pb_{0.988}Sb_{0.012}Te$-14%GeTe. As shown in Figures 3b-d and Table S1 (Supporting Information), this reduction is primarily due to the decrease of the carrier concentration from ~5×10^{19} cm^{-3} to ~1×10^{19} cm^{-3} and Hall mobility from ~365 cm^{2}V^{-1}s^{-1} to ~274 cm^{2}V^{-1}s^{-1}. Moreover, the electrical conductivity monotonically decreases with rising temperature.

As shown in Figures 3b-d and Table S1 (Supporting Information), the carrier concentration and Hall mobility are composition and temperature dependent. The negative Hall coefficients (R_H) confirm the n-type transport behavior (Figure 3b and Figure S2, Supporting Information). The absolute values of the Hall coefficients at 300 K for $Pb_{0.988}Sb_{0.012}Te$-x%GeTe generally increase with x (Figure 3b) indicating that the carrier concentration is reduced at higher x values (Figure 3b, Table S1). One reason for the diminished effectiveness of Sb as an electron donor with rising fraction of GeTe could be the well-known intrinsic Ge vacancies in the lattice as in pure GeTe (x=100).[25] The Hall mobility $\mu_H = \sigma/ne$ is calculated using the electrical conductivity data and presented in Figure 3d and Table S1 (Supporting Information). The Hall mobility for $Pb_{0.988}Sb_{0.012}Te$-x%GeTe-SS decreases with increased GeTe content, likely due to enhanced alloy scattering from increased atomic Pb/Ge disorder. The mobility falls with rising temperature because of charge carrier scattering by acoustic phonons.

Figure 3e presents the Seebeck coefficients of $Pb_{0.988}Sb_{0.012}Te$-x%GeTe-SS in the temperature range of 300 K to 773 K. As expected, the negative Seebeck coefficients indicate n-type charge transport behavior, in agreement with the negative Hall coefficients (Figure 3b and Supporting Information Figure S2) and the donor characteristic of Sb (*i.e.* replacing Pb in the crystal structure). The Seebeck coefficients are enhanced with greater GeTe content. The decrease of the absolute

Seebeck coefficients may be related to the higher carrier concentration above 700 K (Figure 3c) because the excitation of minority carriers will diminish the Seebeck coefficients.[26] The highest absolute value of Seebeck coefficient reached is 300 μVK^{-1} at 723 K for $Pb_{0.988}Sb_{0.012}Te$-13%GeTe-SS.

Figure 3f shows the Seebeck coefficients as a function of charge carrier concentration for $Pb_{0.988}Sb_{0.012}Te$-x%GeTe-SS at 300 K. The solid curves are the theoretical Pisarenko plots for n-type PbTe with effective mass of electrons of 0.3 m_e and 0.4 m_e (m_e is the free electron mass). The experimental data agree well with the theoretical predictions, indicating single band transport in $Pb_{0.988}Sb_{0.012}Te$-x%GeTe-SS. Moreover, the electron effective mass (between $0.3m_e$ and $0.4m_e$) of the GeTe alloyed samples is slightly higher than that (~$0.3m_e$) of $Pb_{0.988}Sb_{0.012}Te$.

The temperature-dependent power factors for $Pb_{0.988}Sb_{0.012}Te$-x%GeTe-SS are presented in Figure 5a. As a consequence of the simultaneous optimization of electrical conductivities and Seebeck coefficients, the Sb doping and GeTe alloying result in high power factors with a maximum value of ~23.3 $\mu Wcm^{-1}K^{-2}$ at $T = 573$ K for the sample with x = 5. Meanwhile, the peak power factor shifts to lower temperature for samples with increased GeTe content, which is beneficial to achieve high ZT values at low temperatures.

2.5. DFT Calculations

We explored the effect of alloying PbTe with GeTe on the electronic band structure using first-principles density functional theory (DFT) calculations. Considering that the dopant Sb atoms only serve for carrier concentration adjustment, the calculated band structures shown here does not include Sb atoms for simplicity. It is shown in Figures 4a and 4b that when Ge atoms are added into PbTe, both the conduction band minimum and valence band maximum move away from the Fermi level leading to an enlarged energy band gap. Compared with pure PbTe, where the calculated band gap is 0.0944 eV, $Pb_{27-n}Ge_nTe_{27}$ shows a 105% larger band gap of 0.1936 eV. The absolute values of the DFT calculated band gaps are usually smaller than those from experimental measurements, in which DFT typically underestimates the band gap values.

The calculated effective masses of both conduction band electrons and valence band holes at the L point are shown in Figure 4c. The calculations suggest that adding Ge into PbTe does not significantly affect the transverse effective masses but remarkably increases the longitudinal ones. We also explored the temperature dependence of the band structures of $Pb_{23}Ge_4Te_{27}$ resulting from only the thermal expansion effect. It can be seen from Figure 4d that the band gap widens when temperature increases, and the effective mass is also enlarged.

2.6. Thermal Transport Properties

The temperature-dependent thermal conductivities of the $Pb_{0.988}Sb_{0.012}Te$-x%GeTe-SS samples are shown in Figure 5b. The introduction of GeTe effectively reduces the thermal conductivity which at room temperature decrease continuously from 4.72 $Wm^{-1}K^{-1}$ to 1.47 $Wm^{-1}K^{-1}$ when x varies from 0 to 14. The heavily doped (*i.e.* x ≥ 10) supersaturated solid solutions possess very low thermal conductivities. The lowest value of 0.82 $Wm^{-1}K^{-1}$ is found in $Pb_{0.988}Sb_{0.012}Te$-14%GeTe at $T = 673$ K. The κ_{lat} is derived by subtracting the electronic component (see Figure S4, Supporting Information) from the total thermal conductivity and is displayed in Figure 5c. The lattice thermal conductivities at

300 K decrease from 2.77 to 1.13 $Wm^{-1}K^{-1}$ when x increases from 0 to 14. Generally, κ_{lat} decreases at higher temperature, except for the samples with x $\geq$ 12, which show a slight rise above 600 K likely due to the increased contribution of bipolar diffusion of holes (minority carriers). Finally, the lowest value of κ_{lat} = 0.61 $Wm^{-1}K^{-1}$ can be achieved for $Pb_{0.988}Sb_{0.012}Te$-13%GeTe-SS at ~573 K. The marked reduction of κ_{lat} is attributed to the multiple types of point defects (such as Ge/Pb, Pb/Ge, Sb/Pb, Pb/Sb, Te/Sb and Sb/Te substitutions). These cause strain and mass contrast between alloying atoms and host atoms in the lattice which serve as scattering centers for phonons.[27]

2.7. Figure of Merit

The dimensionless Figure of merit, *ZT,* values of $Pb_{0.988}Sb_{0.012}Te$-x%GeTe-SS are shown in Figure 5d. The improved power factors and reduced thermal conductivities of Sb-doped PbTe-x%GeTe alloys result in significantly enhanced *ZT* values compared to that of $Pb_{0.988}Sb_{0.012}Te$. Among all samples, $Pb_{0.988}Sb_{0.012}Te$-13%GeTe exhibits the highest *ZT* value of ~1.32 at 623 K (Figure 5d).

2.8. From Solid Solution to Nanostructuring

In general, for PbTe systems different synthesis conditions will lead to different microstructures. The incorporation of nano-scale precipitates in matrix, has been certified as an efficient paradigm to lower lattice thermal conductivities by introducing new scattering mechanisms such as grain boundaries or interfaces without significantly depressing the power factor.[28] To further improve the thermoelectric performance of $Pb_{0.988}Sb_{0.012}Te$-13%GeTe-SS, the low temperature annealing approach (The ingot sample of $Pb_{0.988}Sb_{0.012}Te$-13%GeTe-SS was annealed at 573 K for 2 days, then sintered by SPS at 823 K for 10 min under an axial pressure of 40 MPa) was adopted to introduce the nanoscale precipitates in the PbTe matrix.

Microstructural and chemical analyses of $Pb_{0.988}Sb_{0.012}Te$-13%GeTe-Nano reveal that the presence of large number of nanoscale precipitates varying from 3 to ~100 nm, Figures 6a and 6b. Figures 6c and 6d depict that the precipitates, which are not faceted, adopt the same crystal structure as matrix. Figure 6e shows that the precipitate is rich in Ge and deficient in Pb and probably Te.

The $Pb_{0.988}Sb_{0.012}Te$-13%GeTe-Nano sample exhibits higher electrical conductivity below 423 K (Figure 7a) and larger Seebeck coefficient below 623 K (Figure 7b) than $Pb_{0.988}Sb_{0.012}Te$-13%GeTe-SS sample. As a consequence, a major enhancement of the power factor was achieved for $Pb_{0.988}Sb_{0.012}Te$-13%GeTe-Nano (~15.4 $\mu Wcm^{-1}K^{-2}$), about 70% improvement over $Pb_{0.988}Sb_{0.012}Te$-13%GeTe-SS (~9.3 $\mu Wcm^{-1}K^{-2}$) at room temperature (Figure 7c). The $Pb_{0.988}Sb_{0.012}Te$-13%GeTe-Nano has lower κ_{tot} and κ_{lat} values than $Pb_{0.988}Sb_{0.012}Te$-13%GeTe-SS over the entire measured temperature range (Figures 7d and 7e). A very low-value of κ_{lat} = 0.56 $Wm^{-1}K^{-1}$ can be achieved for $Pb_{0.988}Sb_{0.012}Te$-13%-Nano at ~573 K. As a result, $Pb_{0.988}Sb_{0.012}Te$-13%GeTe-Nano exhibits a higher *ZT* value of ~1.38 at 623 K (Figure 7f). Compared with the maximum *ZT* value (0.58) of $Pb_{0.988}Sb_{0.012}Te$, the $Pb_{0.988}Sb_{0.012}Te$-13%GeTe-Nnao pellet achieves ~140% improvement of the maximum *ZT* value. This high thermoelectric *ZT* value outperforms many n-type PbTe reported so far especially at the low temperature range (300 K to 800 K).[18, 29] Furthermore, the average ZT_{avg} value of ~1.04 is obtained in the temperature range from 300 K to 773 K (Figure 8) for $Pb_{0.988}Sb_{0.012}Te$-13%GeTe-Nano, which is higher than the average ZT_{avg} values reported for n-type PbTe.[18, 23, 29a, 30]

3. Summary and Conclusion

The thermoelectric performance of n-type PbTe samples can be significantly improved by alloying with GeTe. Both supersaturated solid solutions and nanostructured $Pb_{1-x}Ge_xTe$ systems can be prepared *via* a non-equilibrium process. The experimental and theoretical analyses reveal that (i) GeTe alloying enlarges the band gap and electron effective mass leading to a considerable enhancement of the Seebeck coefficient; (ii) the carrier concentrations can be optimized in the range of ~1 to 5×10^{19} cm^{-3}, by controlling the GeTe fraction to achieve high *ZT* values; (iii) the high density of point defects resulting from the supersaturated state using the non-equilibrium synthetic route described above leads to greatly decreased κ_{lat}. Moreover, the formation of nanostructures can further improve the power factor and reduce κ_{lat} simultaneously. The $Pb_{0.988}Sb_{0.012}$Te-13%GeTe-Nano achieves a *ZT* value of 1.38 at 623 K and a high average *ZT*$_{avg}$ value of ~1.04 in the temperature range of 300 K to 773 K, which is promising for intermediate temperature thermoelectric applications.

4. Experimental Section

The following chemicals were used in this work: Pb wire (99.99%, American Elements, USA), Te shot (99.999%, 5 N Plus, Canada), Sb (99.999%, American Elements, USA), Ge lump (99.999%, Plasmaterials, USA). A mixture of high-purity single elements Pb, Sb, Ge and Te was loaded into quartz tubes according to the stoichiometric molar ratios of $Pb_{0.988}Sb_{0.012}$Te-x%GeTe (x = 0, 2, 5, 8, 10, 12, 13 and 14). The Sb-free PbTe-x%GeTe compounds were synthesized for optical band gap measurements. After loading the quartz tubes, the quartz tubes were evacuated to a residual pressure of ~10^{-4} torr and flame-sealed. Next, they were heated up to 1323 K in 10 h and held at this temperature for 6 h, then quenched in ice water and annealed at 873 K for 2 days. For the $Pb_{0.988}Sb_{0.012}$Te-13%GeTe-Nano samples, the annealing temperature was 573 K. The obtained ingots were hand ground to a powder using a mechanical mortar and pestle to reduce the particle sizes to less than 53 μm^3 in a N$_2$-filled glove box. Then these powders were densified under vacuum using spark plasma sintering (SPS) technique (SPS-211LX, Fuji Electronic Industrial Co. Ltd.) at 823 K for 10 min in a 12.7 mm diameter graphite die under an axial pressure of 40 MPa. Highly dense (> 96% of theoretical density) disk-shaped pellets with size of ~10 mm in thickness and 12.7 mm in diameter were obtained.

Powder X-ray Diffraction (PXRD) patterns were collected on finely ground powders for all samples using a Rigaku Miniflex powder X-ray diffractometer with Ni-filtered Cu K$_\alpha$ (λ = 1.5418 Å) radiation operating at 40 kV and 15 mA. The scan width and rate of the measurement was 0.02° and 10 °/min, respectively.

The optical band gaps of PbTe-x%GeTe were measured on finely ground samples at 300 K. The spectra were recorded in the mid-IR range (6000−400 cm^{-1}) using a Nicolet 6700 FT-IR spectrometer. The optical band gaps were converted from reflectance spectra using Kubelka-Munk equations: $\alpha/S' = (1−R)^2/(2R)$, where R, α and S' are reflectance, absorption and scattering coefficients, respectively.[31]

The obtained SPSed pellets were cut into rectangular bars with dimensions ~12 mm × 3 mm × 3 mm that were used for simultaneous measurement of the electrical resistivity and Seebeck coefficient. The measurements were performed with an Ulvac Riko ZEM-3 instrument under a low-pressure helium atmosphere from 300 K to 773 K. To avoid elemental sublimation and to protect the instrument,

the bars were coated with a thin layer of boron nitride (BN). The measurement uncertainties typically are 5% for electrical resistivity and 3% for the Seebeck coefficient, respectively.[32]

The Hall effect measurements were carried out using an AC 4-probe method in a homemade system mainly using fields of 0.5 and −0.5 Tesla. The homemade system uses an air-bore, helium-cooled superconducting magnet to generate the field within a high temperature oven that surrounds the Ar-filled sample probe. The Hall bars had dimensions ~1 mm × 3 mm × 8 mm. The error in the Hall coefficient was estimated from the noise in the signal and from the standard deviation of multiple measurements at a given temperature. The carrier concentration was calculated assuming a single carrier *via* $n = 1/(e|R_H|)$, where e is the electronic charge and R_H is the Hall coefficient, with the error propagated from the Hall coefficient.

Thermal diffusivity measurements were performed on highly dense SPSed pellets which were cut and polished into a squared shape of ~6 mm × 6 mm × 2 mm. Then the samples were coated with a thin layer of graphite to minimize errors from the emissivity of the material. The temperature-dependent thermal conductivity was then calculated with the relationship of $\kappa = D \cdot C_p \cdot \rho$. In this formula, D is the thermal diffusivity (measured using the laser flash diffusivity method in a Netzsch LFA457 under nitrogen atmosphere and analyzed using a Cowan model with pulse correction), C_p is the specific heat capacity (determined by the formula C_p (k_B per atom) = 3.07 + 4.7 × 10^{-4} × (T(/K) − 300); here, k_B is the Boltzmann constant),[30a] and ρ is the bulk density (calculated using the dimensions and mass, see Table S2, Supporting Information). Considering the uncertainties of 5% for D and 5% for ρ, the uncertainty of the thermal conductivity is estimated to be within 7%. Thus, the combined uncertainty for all measurements involved in the determination of ZT is about 15~20%.

Scanning/Transmission Electron Microscopy (S/TEM) investigations were carried out for $Pb_{0.988}Sb_{0.012}Te$-13%GeTe-SS and $Pb_{0.988}Sb_{0.012}Te$-13%GeTe-Nano systems. Conventional and high-resolution TEM, as well as Selective Area Electron Diffraction (SAED) were performed with a JEOL 2100F transmission electron microscope under 200 kV. High Angle Annular Dark Field (HAADF) STEM imaging and Energy Dispersive X-ray Spectroscopy (EDS) were performed with a Hitachi HD-2300 Dual EDS Cryo STEM operated under 200 kV. The TEM specimen was prepared with conventional methods, including dicing, grinding, dimpling, followed by high energy (2.8 keV) Ar ion milling until hole formation and cleaned with 2 keV and then low energy (300 eV) Ar ion milling. Ar ion milling was performed with a Fischione Model 1050 TEM Mill at cryogenic temperature with the help of a liquid nitrogen cooling stage. Scanning electron microscopy (SEM) and EDS analysis were performed for $Pb_{0.988}Sb_{0.012}Te$-13%GeTe-Nano before the SPS process using a Hitachi S-3400N-II SEM with a solid state backscattered electron (BSE) detector.

Density Functional Theory (DFT)[33] band structure calculations were carried out for pure stoichiometric PbTe and GeTe alloyed PbTe. The calculations were performed using the Vienna *ab initio* Simulation Package (VASP)[34] with projector augmented wave (PAW)[35] pseudopotentials utilizing the generalized gradient approximation and Perdew-Burke-Ernzerhof (PBE)[36] exchange-correlation. For Pb and Ge atoms, the semi core d electrons were treated as valence states. Both relaxation calculations and band structure calculations were performed with a plane-wave basis cutoff energy of 520 eV and spin-orbit coupling (SOC). The total energies were converged within 0.01 meV with a Monkhorst-Pack[37] k-mesh with 5000 k-points per reciprocal atom in the Brillouin zone.

WILEY-VCH

Supporting Information

Supporting Information is available from the Wiley Online Library or from the author.

Received: ((will be filled in by the editorial staff))
Revised: ((will be filled in by the editorial staff))
Published online: ((will be filled in by the editorial staff))

References

[1]   a) L. D. Zhao, S. H. Lo, Y. Zhang, H. Sun, G. Tan, C. Uher, C. Wolverton, V. P. Dravid, M. G.

Kanatzidis, *Nature* **2014**, *508*, 373; b) Y. Pei, X. Shi, A. LaLonde, H. Wang, L. Chen, G. J. Snyder, *Nature*

2011, *473*, 66; c) K. Biswas, J. He, I. D. Blum, C.-I. Wu, T. P. Hogan, D. N. Seidman, V. P. Dravid, M. G.

Kanatzidis, *Nature* **2012**, *489*, 414; d) Q. H. Zhang, X. Y. Huang, S. Q. Bai, X. Shi, C. Uher, L. D. Chen,

Adv. Eng. Mater. **2016**, *18*, 194; e) Y. Zhou, L. D. Zhao, *Adv. Mater.*, DOI:

10.1002/adma.2017026761702676.

[2]   a) G. Tan, L.-D. Zhao, M. G. Kanatzidis, *Chem. Rev.* **2016**, *116*, 12123; b) Y. Luo, Y. Zheng, Z.

Luo, S. Hao, C. Du, Q. Liang, Z. Li, K. A. Khor, K. Hippalgaonkar, J. Xu, Q. Yan, C. Wolverton, M. G.

Kanatzidis, *Adv. Eng. Mater.* **2018**, *8*, 1702167.

[3]   A. S. Rattner, S. Garimella, *Energy* **2011**, *36*, 6172.

[4]   a) O. Delaire, J. Ma, K. Marty, A. F. May, M. A. McGuire, M. H. Du, D. J. Singh, A. Podlesnyak,

G. Ehlers, M. D. Lumsden, B. C. Sales, *Nat. Mater.* **2011**, *10*, 614; b) S. Lee, K. Esfarjani, T. Luo, J.

Zhou, Z. Tian, G. Chen, *Nat. Commun.* **2014**, *5*, 3525; c) E. S. Božin, C. D. Malliakas, P. Souvatzis, T.

Proffen, N. A. Spaldin, M. G. Kanatzidis, S. J. L. Billinge, *Science* **2010**, *330*, 1660.

[5]   H. Sitter, K. Lischka, H. Heinrich, *Phys. Rev. B* **1977**, *16*, 680.

[6]   a) L. D. Zhao, H. J. Wu, S. Q. Hao, C. I. Wu, X. Y. Zhou, K. Biswas, J. Q. He, T. P. Hogan, C. Uher,

C. Wolverton, V. P. Dravid, M. G. Kanatzidis, *Energy Environ. Sci.* **2013**, *6*, 3346; b) Z. Jian, Z. Chen, W.

Li, J. Yang, W. Zhang, Y. Pei, *J. Mater. Chem. C* **2015**, *3*, 12410; c) H. J. Wu, L. D. Zhao, F. S. Zheng, D.

Wu, Y. L. Pei, X. Tong, M. G. Kanatzidis, J. Q. He, *Nat. Commun.* **2014**, *5*, 4515; d) J. Androulakis, I.

Todorov, D.-Y. Chung, S. Ballikaya, G. Wang, C. Uher, M. Kanatzidis, *Phys. Rev. B* **2010**, *82*, 115209; e)

Q. Zhang, F. Cao, W. Liu, K. Lukas, B. Yu, S. Chen, C. Opeil, D. Broido, G. Chen, Z. Ren, *J. Am. Chem.*

Soc. **2012**, *134*, 10031; f) Y. Pei, A. D. LaLonde, N. A. Heinz, G. J. Snyder, *Adv. Eng. Mater.* **2012**, *2*,

670; g) A. Łusakowski, P. Bogusławski, T. Radzyński, *Phys. Rev. B* **2011**, *83*, 115206.

[7]   a) Q. Zhang, H. Wang, W. Liu, H. Wang, B. Yu, Q. Zhang, Z. Tian, G. Ni, S. Lee, K. Esfarjani, G.

Chen, Z. Ren, *Energy Environ. Sci.* **2012**, *5*, 5246; b) J. P. Heremans, V. Jovovic, E. S. Toberer, A.

Saramat, K. Kurosaki, A. Charoenphakdee, S. Yamanaka, G. J. Snyder, *Science* **2008**, *321*, 554.

[8]   Y. Tang, Z. M. Gibbs, L. A. Agapito, G. Li, H.-S. Kim, M. B. Nardelli, S. Curtarolo, G. J. Snyder,

Nat. Mater. **2015**, *14*, 1223.

[9]   a) K. Ahn, K. Biswas, J. He, I. Chung, V. Dravid, M. G. Kanatzidis, *Energy Environ. Sci.* **2013**, *6*,

1529; b) L. D. Zhao, J. He, C. I. Wu, T. P. Hogan, X. Zhou, C. Uher, V. P. Dravid, M. G. Kanatzidis, *J. Am.

Chem. Soc.* **2012**, *134*, 7902.

[10]   S. A. Yamini, H. Wang, Z. M. Gibbs, Y. Pei, S. X. Dou, G. J. Snyder, *Phys. Chem. Chem. Phys.*

2014, *16*, 1835.

[11]   K. Biswas, J. He, Q. Zhang, G. Wang, C. Uher, V. P. Dravid, M. G. Kanatzidis, *Nat. Chem.* **2011**,

3, 160.

[12]   a) H. Xie, H. Wang, Y. Pei, C. Fu, X. Liu, G. J. Snyder, X. Zhao, T. Zhu, *Adv. Funct. Mater.* **2013**,

23, 5123; b) J. Li, H. Wu, D. Wu, C. Wang, Z. Zhang, Y. Li, F. Liu, W.-q. Ao, J. He, *Chem. Mater.* **2016**,

28, 6367; c) G. Tan, F. Shi, S. Hao, L.-D. Zhao, H. Chi, X. Zhang, C. Uher, C. Wolverton, V. P. Dravid, M.

G. Kanatzidis, *Nat. Commun.* **2016**, *7*, 12167; d) Y. Lee, S. H. Lo, C. Chen, H. Sun, D. Y. Chung, T. C.

Chasapis, C. Uher, V. P. Dravid, M. G. Kanatzidis, *Nat. Commun.* **2014**, 5, 3640.

[13]   Y. Takagiwa, Y. Pei, G. Pomrehn, G. J. Snyder, *APL Mater.* **2013**, *1*, 011101.

[14]   H. Wang, Y. Pei, A. D. LaLonde, G. J. Snyder, *Proc. Natl. Acad. Sci. U.S.A.* **2012**, *109*, 9705.

[15]   a) A. Popescu, A. Datta, G. S. Nolas, L. M. Woods, *J. Appl. Phys.* **2011**, *109*, 103709; b) K. Kengo, Y. Kazuo, K. Tsuyoshi, *Jpn. J. Appl. Phys.* **2003**, *42*, 501; c) X. Hu, P. Jood, M. Ohta, M. Kunii, K. Nagase, H. Nishiate, M. G. Kanatzidis, A. Yamamoto, *Energy Environ. Sci.* **2016**, *9*, 517.

[16]   M. Guch, C. R. Sankar, J. R. Salvador, G. P. Meisner, H. Kleinke, *J. Appl. Phys.* **2012**, *111*, 063706.

[17]   S. Aminorroaya Yamini, H. Wang, D. Ginting, D. R. G. Mitchell, S. X. Dou, G. J. Snyder, *ACS Appl. Mater. Interfaces* **2014**, *6*, 11476.

[18]   Q. Zhang, E. K. Chere, Y. Wang, H. S. Kim, R. He, F. Cao, K. Dahal, D. Broido, G. Chen, Z. Ren, *Nano Energy* **2016**, *22*, 572.

[19]   Y. Xiao, H. Wu, W. Li, M. Yin, Y. Pei, Y. Zhang, L. Fu, Y. Chen, S. J. Pennycook, L. Huang, J. He, L. D. Zhao, *J. Am. Chem. Soc.* **2017**, *139*, 18732.

[20]   a) H. Okamoto, *J. Phase Equilib.* **2000**, *21*, 496; b) G. C. Christakudis, S. K. Plachkova, L. E. Shelimova, E. S. Avilov, *Phys. Status Solidi A* **1991**, *128*, 465; c) B. A. Cook, M. J. Kramer, X. Wei, J. L. Harringa, E. M. Levin, *J. Appl. Phys.* **2007**, *101*, 053715; d) B. Dado, Y. Gelbstein, D. Mogilansky, V. Ezersky, M. P. Dariel, *J. Electron. Mater.* **2010**, *39*, 2165.

[21]   a) Y. Gelbstein, J. Davidow, S. N. Girard, D. Y. Chung, M. Kanatzidis, *Adv. Energy Mater.* **2013**, *3*, 815; b) Y. Gelbstein, Z. Dashevsky, M. P. Dariel, *Phys. Status Solidi RRL* **2007**, 1, 232; c) E. Hazan, O. Ben-Yehuda, N. Madar, Y. Gelbstein, *Adv. Energy Mater.* **2015**, *5*, 1500272.

13

[22]   a) I. Kudman, *Metall. Trans.* **1971**, *2*, 163; b) V. N. Vodop'yanov, A. P. Bakhtinov, E. I. Slyn'ko, M. V. Radchenko, V. I. Sichkovskyi, G. V. Lashkarev, W. Dobrowolski, R. Yakiela, *Phys. Solid State* **2006**, *48*, 1342.

[23]   G. Tan, C. C. Stoumpos, S. Wang, T. P. Bailey, L. D. Zhao, C. Uher, M. G. Kanatzidis, *Adv. Energy Mater.* **2017**, *7*, 1700099.

[24]   R. Tsu, W. E. Howard, L. Esaki, *Solid State Commun.* **1967**, *5*, 167.

[25]   D. H. Damon, M. S. Lubell, R. Mazelsky, *J. Phys. Chem. Solids* **1967**, *28*, 520.

[26]   J. H. Bahk, A. Shakouri, *Phys. Rev. B* **2016**, *93*, 165209.

[27]   H. Wang, A. D. LaLonde, Y. Pei, G. J. Snyder, *Adv. Funct. Mater.* **2013**, *23*, 1586.

[28]   M. G. Kanatzidis, *Chem. Mater.* **2010**, *22*, 648.

[29]   a) P. Jood, M. Ohta, M. Kunii, X. Hu, H. Nishiate, A. Yamamoto, M. G. Kanatzidis, *J. Mater. Chem. C* **2015**, *3*, 10401; b) S. N. Girard, T. C. Chasapis, J. He, X. Zhou, E. Hatzikraniotis, C. Uher, K. M. Paraskevopoulos, V. P. Dravid, M. G. Kanatzidis, *Energy Environ. Sci.* **2012**, *5*, 8716.

[30]   a) Y. Pei, Z. M. Gibbs, A. Gloskovskii, B. Balke, W. G. Zeier, G. J. Snyder, *Adv. Energy Mater.* **2014**, *4*, 1400486; b) G. Komisarchik, D. Fuks, Y. Gelbstein, *J. Appl. Phys.* **2016**, *120*, 055104.

[31]   T. J. McCarthy, S. P. Ngeyi, J. H. Liao, D. C. DeGroot, T. Hogan, C. R. Kannewurf, M. G. Kanatzidis, *Chem. Mater.* **1993**, *5*, 331.

[32]   K. A. Borup, J. de Boor, H. Wang, F. Drymiotis, F. Gascoin, X. Shi, L. Chen, M. I. Fedorov, E. Muller, B. B. Iversen, G. J. Snyder, *Energy Environ. Sci.* **2015**, *8*, 423.

[33]   a) P. Hohenberg, W. Kohn, *Phys. Rev.* **1964**, *136*, B864; b) W. Kohn, L. J. Sham, *Phys. Rev.* **1965**, *140*, A1133.

[34]   G. Kresse, J. Furthmüller, *Phys. Rev. B* **1996**, *54*, 11169.

[35]   P. E. Blöchl, *Phys. Rev. B* **1994**, *50*, 17953.

[36]   J. P. Perdew, K. Burke, M. Ernzerhof, *Phys. Rev. Lett.* **1996**, *77*, 3865.

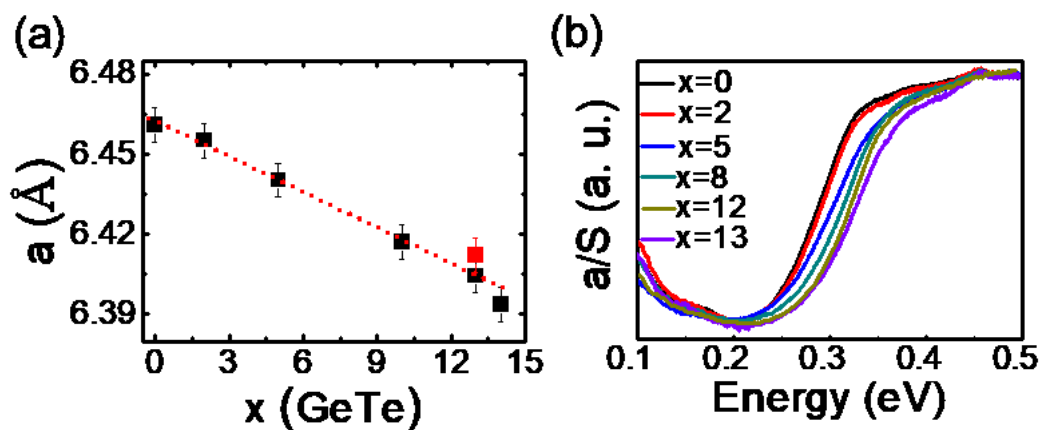[37]   H. J. Monkhorst, J. D. Pack, *Phys. Rev. B* **1976**, *13*, 5188.

Figures

Figure. 1. (a) Refined lattice parameters of $Pb_{0.988}Sb_{0.012}Te$-x%GeTe-SS (black) and $Pb_{0.988}Sb_{0.012}Te$-13%GeTe-Nano (red) as a function of GeTe content, indicating a linear contraction of the lattice. The red short dotted line is the Vegard's law type behavior and (b) Electronic absorption spectra obtained from diffuse reflectance infrared spectroscopy measurements on PbTe-x%GeTe samples (without Sb doping to minimize interband states), showing increasing band gap with increasing GeTe content.
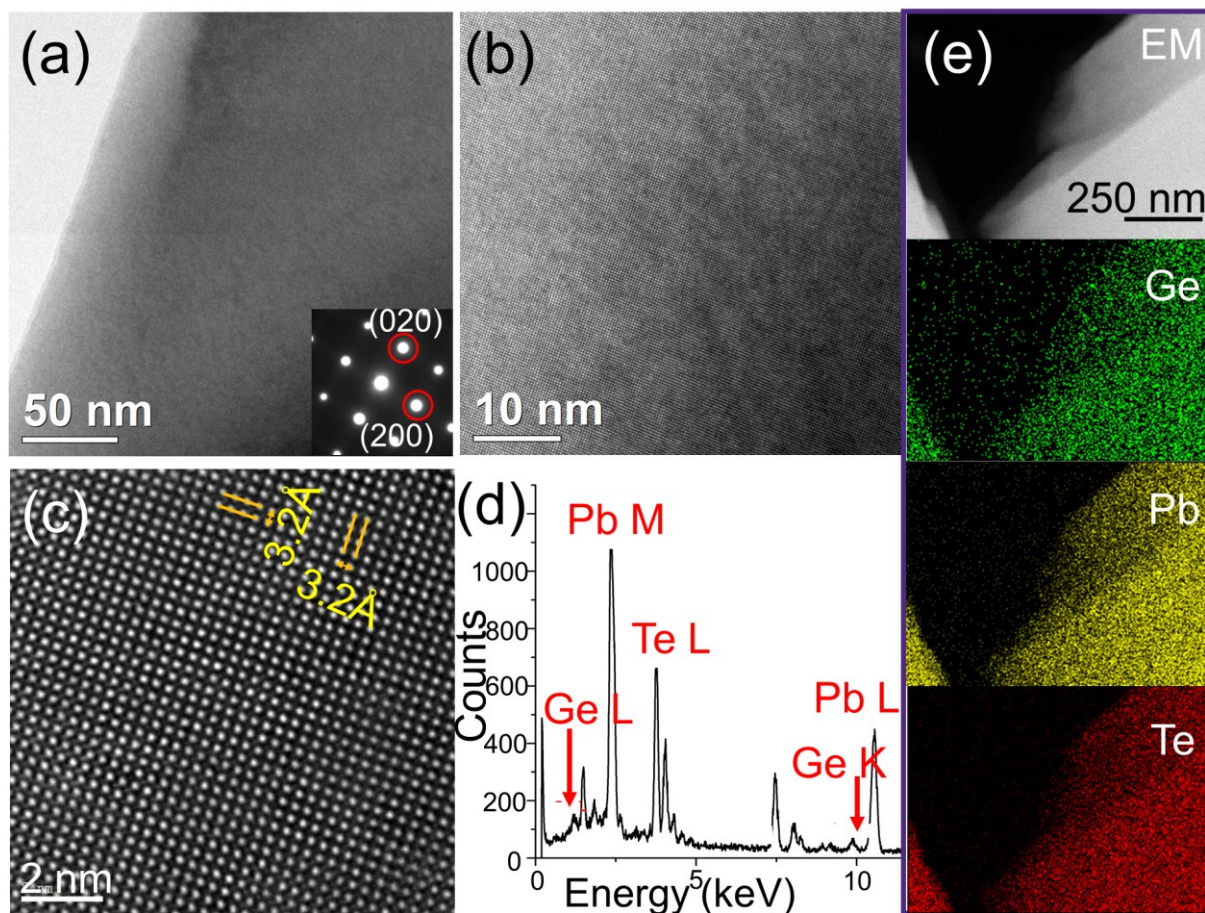
Figure. 2. S/TEM and EDS analysis of $Pb_{0.988}Sb_{0.012}Te$-13%GeTe-SS. (a) Low magnification; (b) medium magnification and (c) high-resolution TEM images show a homogeneous, single-phase solid solution. No obvious nanostructures can be observed. Selective area electron diffraction (SAED) pattern is shown in the inset image of (a). No streaking or spot splitting can be observed in SAED pattern, indicating the solid-solution nature of the material; (d) EDS spectrum of $Pb_{0.988}Sb_{0.012}Te$-13%GeTe-SS, indicating the existence of Pb, Te and Ge elements in the sample. The unlabeled peaks come from the TEM specimen holder or the TEM grid underneath the sample; and (e) STEM HAADF image and elemental EDS mapping of $Pb_{0.988}Sb_{0.012}Te$-13%GeTe-SS. Ge, Pb, and Te distribute uniformly in the sample, the contrast difference in elemental maps is due to sample thickness variations.
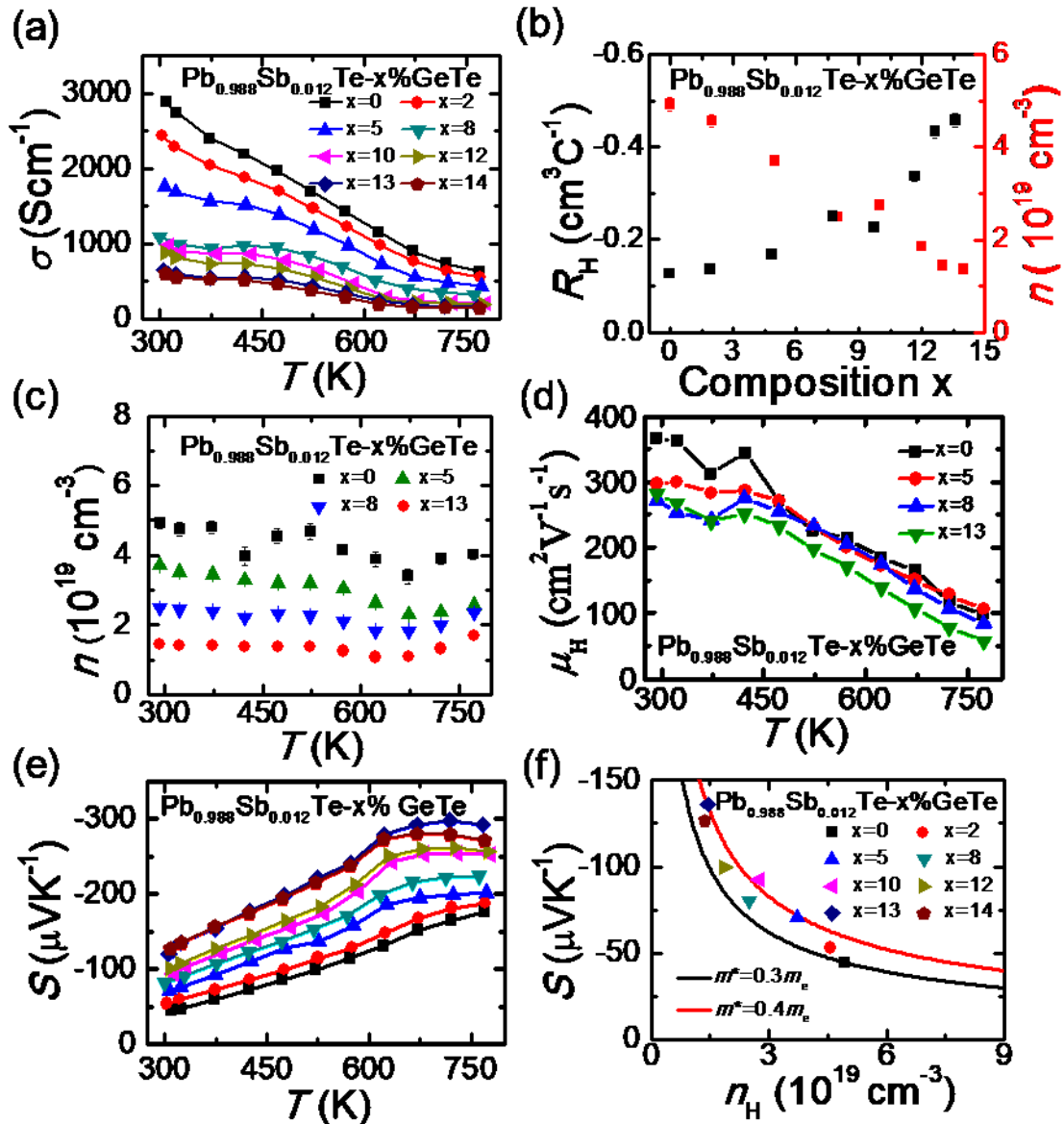
Figure. 3. Thermoelectric transport properties as a function of temperature for $Pb_{0.988}Sb_{0.012}Te$-x%GeTe-SS SPSed pellets; (a) Electrical conductivity, σ; (b) Hall coefficient, R_H and carrier concentration, n at 300 K; (c) The temperature-dependence of carrier concentration for $Pb_{0.988}Sb_{0.012}Te$-x%GeTe-SS (x = 0, 5, 8, and 13); (d) corresponding Hall mobility; (e) Seebeck coefficient, S; and (f) Seebeck coefficient as a function of Hall carrier concentration at 300 K. The solid curves are the theoretical Pisarenko plots for n-type PbTe with effective mass of electrons of 0.3 m_e (black) and 0.4 m_e (red).
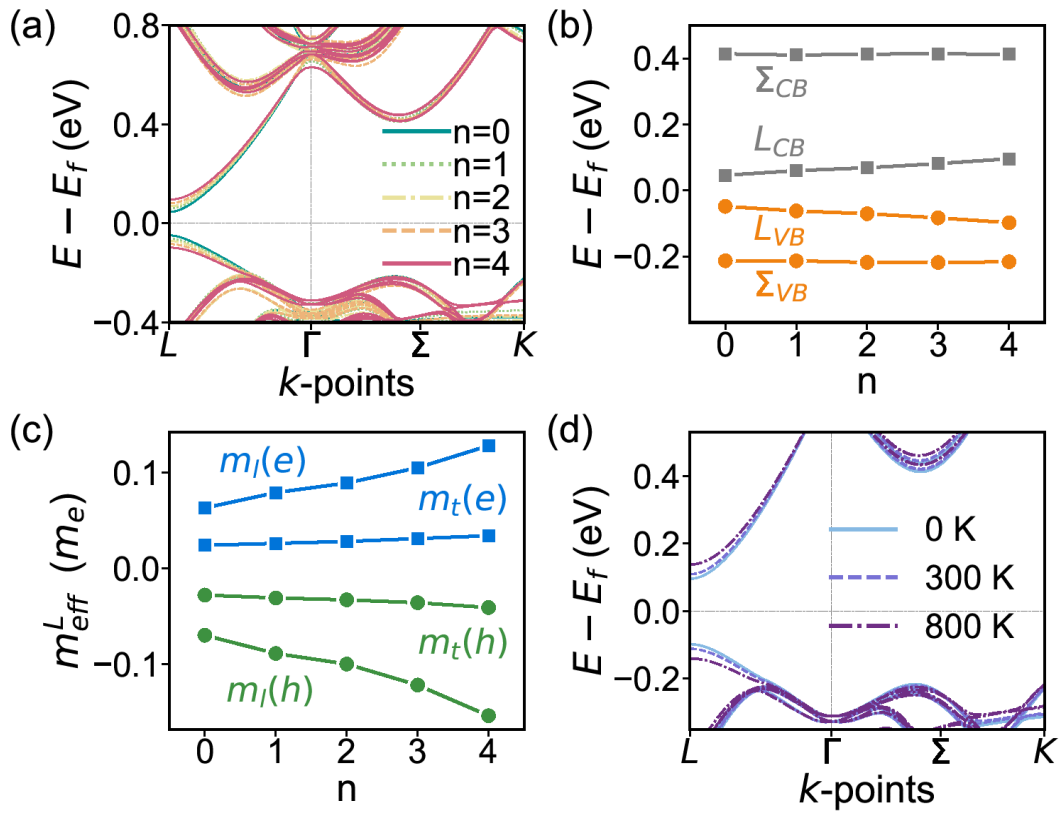
Figure. 4. (a) Calculated electronic band structures of $Pb_{27-n}Ge_nTe_{27}$ (n = 0, 1, 2, 3 and 4), with spin-orbit coupling included; (b) Calculated band-edge energies of the conduction band (CB) and valence band (VB) at L and Σ, as functions of n in $Pb_{27-n}Ge_nTe_{27}$; (c) Calculated effective masses (longitudinal m_l, transverse m_t) of electrons (e) and holes (h) at the L point in reciprocal space as functions of n in $Pb_{27-n}Ge_nTe_{27}$. The unit m_e is the free electron mass; (d) Temperature-dependence of the calculated band structures of $Pb_{23}Ge_4Te_{27}$ considering only the thermal expansion effect.
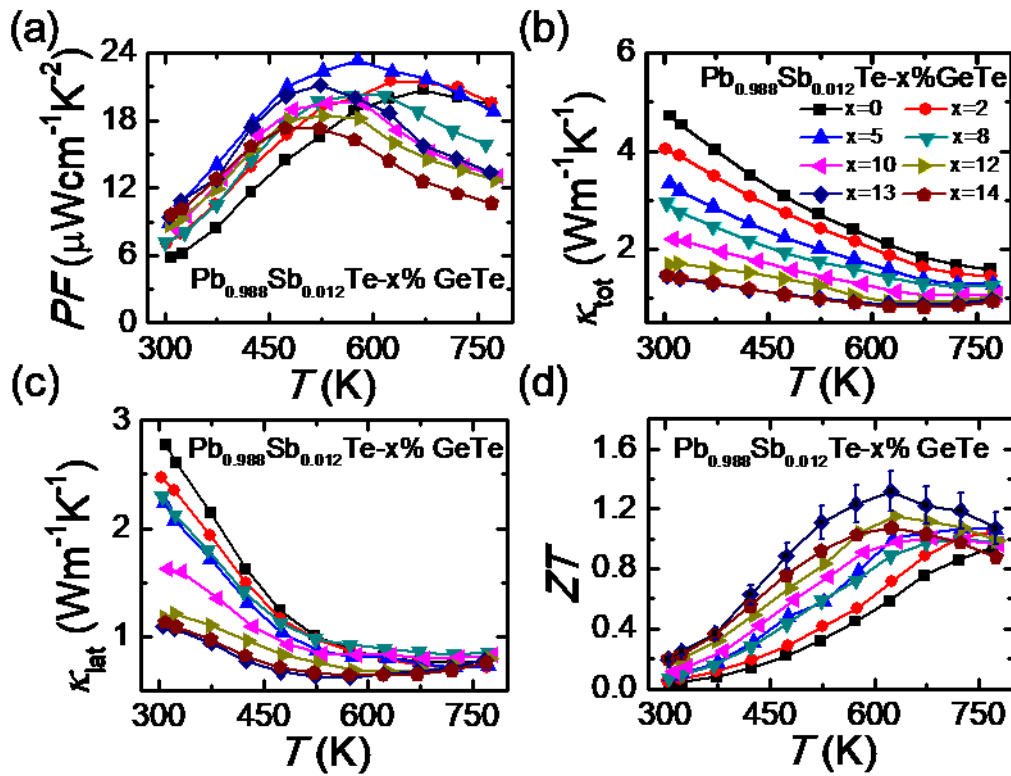
Figure. 5. (a) Power factors, *PF*; (b) Total thermal conductivity, κ_{tot}; (c) Lattice thermal conductivity, κ_{lat}; and (d) Figure of merit, *ZT,* values for $Pb_{0.988}Sb_{0.012}Te$-x%GeTe-SS SPSed pellets.
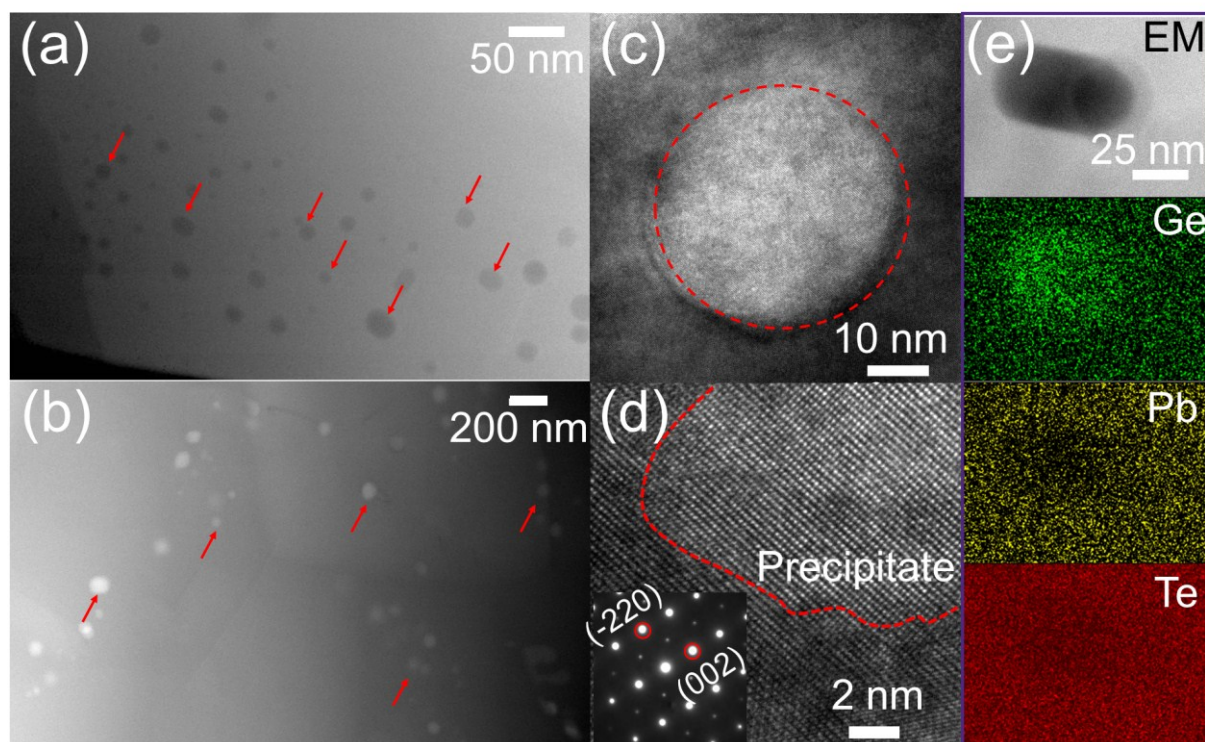
Figure. 6. S/TEM and EDS analysis of $Pb_{0.988}Sb_{0.012}Te$-13%GeTe-Nano. (a) STEM HAADF image and (b) STEM ADF image of $Pb_{0.988}Sb_{0.012}Te$-13%GeTe-Nano system. Large number density of nanoscale precipitates (selectively indicated by red arrows) can be observed; (c) conventional medium magnification TEM image of a representative precipitate (outlined by the red circle); (d) high-resolution TEM image of a representative precipitate-matrix interface. The precipitate was indicated by the red dashed line. Selective area electron diffraction (SAED) pattern is shown as the inset image at the lower left corner; and (e) STEM HAADF image and elemental EDS mapping of a representative area in $Pb_{0.988}Sb_{0.012}Te$-13%GeTe-Nano. The maps demonstrate that the precipitate has higher Ge concentration and lower Pb, Te concentrations than the matrix.
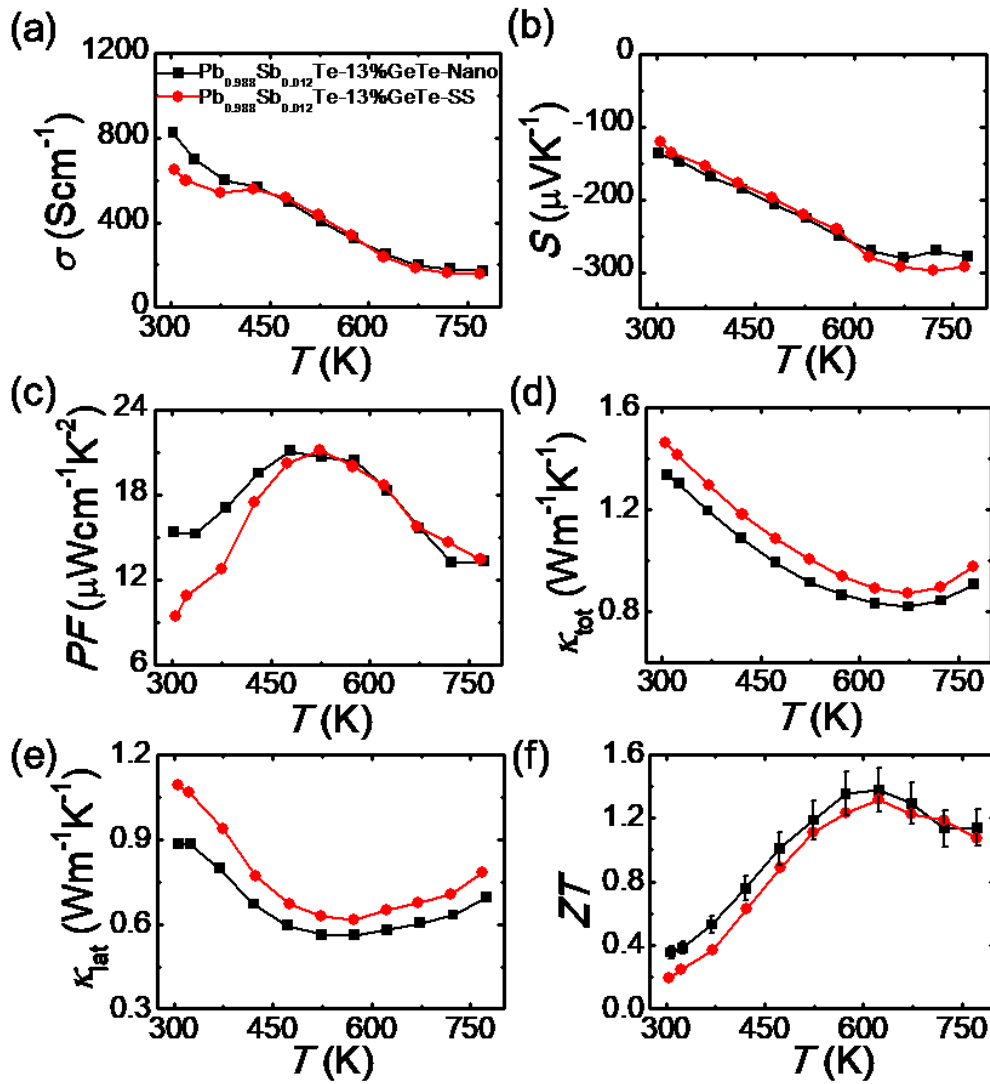
Figure. 7. Thermoelectric transport properties as a function of temperature for $Pb_{0.988}Sb_{0.012}Te$-13%GeTe-SS and $Pb_{0.988}Sb_{0.012}Te$-13%GeTe-Nano SPSed pellets; (a) Electrical conductivity; (b) Seebeck coefficient; (c) Power factor; (d) Total thermal conductivity; (e) Lattice thermal conductivity; and (f) ZT values.
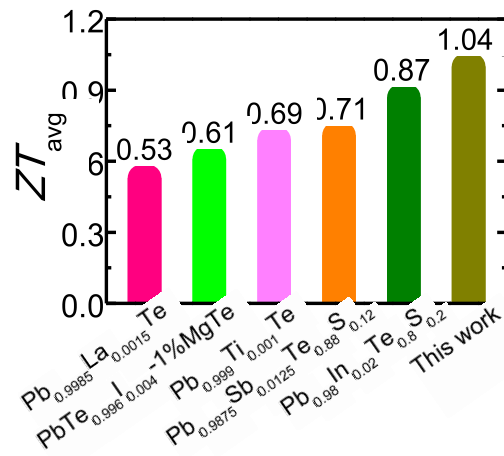
Figure. 8. Comparison of average ZT_{avg} values with the temperature gradient of 300 K to 773 K for several n-type PbTe thermoelectric materials.

The table of contents:

Both supersaturated solid solutions and nanostructured n-type $Pb_{1-x}Ge_xTe$ systems can be prepared *via* a non-equilibrium process with excellent thermoelectric performance. The nanostructured sample can further enhance the *ZT via* reducing the lattice thermal conductively. Then the ZT_{avg} of ~1.04 is obtained, which is among the highest ZT_{avg} values for n-type PbTe materials reported so far.
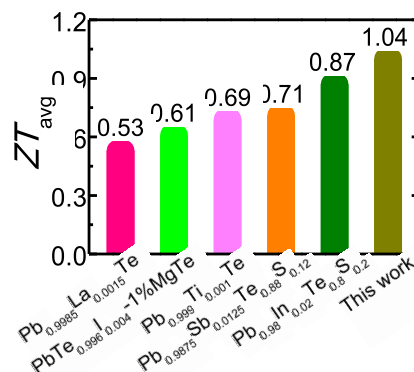
Keyword

thermoelectric, n-type PbTe, GeTe alloying, thermal conductivity

Zhong-Zhen Luo, Xiaomi Zhang, Xia Hua, Gangjian Tan, Trevor P. Bailey, Jianwei Xu, Ctirad Uher, Chris Wolverton, Vinayak P. Dravid, Qingyu Yan,* Mercouri G. Kanatzidis*

Title

High Thermoelectric Performance in Supersaturated Solid Solutions and Nanostructured n-type PbTe-GeTe

ToC figure